

# Optimal Field-Effect Transistor Operation for High-Resolution Biochemical Measurements

Son T Le<sup>1,2</sup>, Seulki Cho<sup>3</sup>, Curt A. Richter<sup>1</sup>, Arvind Balijepalli<sup>3,\*</sup>

<sup>1</sup>Alternative Computing Group, Nanoscale Device Characterization Division, National Institute of Standards and Technology, Gaithersburg, MD 20899, USA

<sup>2</sup>Theiss Research, La Jolla, CA 92037, USA

<sup>3</sup>Biophysics Group, Microsystems and Nanotechnology Division, National Institute of Standards and Technology, Gaithersburg, MD 20899, USA

\*e-mail: arvind.balijepalli@nist.gov

## Abstract

Field-effect transistors (FETs) are powerful tools for sensitive measurements of numerous biomarkers (e.g., proteins, nucleic acids, antigen, etc.) and gaseous species. Most research in the field has focused on building discrete devices with high performance. We show that instrumentation that is commonly used in multiple areas of physics and engineering can greatly improve the performance of measurement systems that embed FET-based transducers for biological applications. We review the state-of-the-art instrumentation in the field as applied to sensing with FETs. We show how high-performance dual-gate 2D FETs that we recently developed, when operated using closed-loop proportional-integral-derivative (PID) control, can drastically improve both sensitivity and resolution. We further show that this closed-loop control approach can be extended to commonly used single-gate silicon FETs. The generalizability of the results will allow their application to virtually any previously developed FET-based sensor. Finally, we provide insights into further optimization and performance benefits that can be extracted by using the closed-loop feedback approach for applications in biosensing.

## 1. Introduction

Chipscale biochemical sensing devices are increasingly being used in medical diagnostics,<sup>1</sup> remote environmental monitoring,<sup>2,3</sup> food security,<sup>4</sup> and drug discovery.<sup>5</sup> In the most general sense, biochemical measurement devices convert a biological interaction between an analyte of interest and a recognition element that imparts specificity into a quantifiable and processable signal. Typical biochemical sensing systems consist of a membrane with an analyte sensitive bioreceptor, an efficient transducer, and signal processing elements. The performance of these systems depends on several elements in the measurement chain, as seen in Figure 1. The bioreceptor must have an extremely high affinity for the analyte being measured, be stable under normal storage conditions, and exhibit low variation between assays. The response of the transducer should be accurate, precise, and reproducible over the usable dynamic range. Finally, the measured interactions should be specific for the target reaction and insensitive to other confounding physical and chemical environmental effects.

A common approach to improve the performance of electronic biochemical measurements is to enhance signal transduction with the goal of increasing sensitivity. The approaches have led to the development of field-effect transistors (FETs) that utilize one-dimensional (1D) materials such as silicon nanowires (SiNWs) and carbon nanotubes (CNTs). These devices enable high sensitivity measurements of the

surface potential of biomolecules when they adsorb to the gate dielectric of the FETs. A key advantage of utilizing 1D materials is the drastic increase in sensitivity due to the high surface-to-volume ratio of the structures over conventional nanoplate devices, which allows a large change in the channel current per unit adsorbed charge. But this improved sensitivity comes at the cost severe fabrication and integration challenges, which limit the availability and adoption of these devices for biomedical applications. Recent advances in the discovery and engineering of atomic scale two-dimensional (2D) materials such as semi-metallic graphene, insulating hexagonal boron nitride (hBN) and semiconducting transition metal dichalcogenides (TMDs), such as molybdenum disulfide ( $\text{MoS}_2$ ), tungsten disulfide ( $\text{WS}_2$ ) or tungsten diselenide ( $\text{WSe}_2$ ) that can have a direct energy band gap for monolayer films<sup>6</sup> and theoretical mobilities as high as  $1,000 \text{ cm}^2 \text{ V}^{-1} \text{ s}^{-1}$  at room temperature, have made a new palette of materials available.<sup>7</sup> These have shown great promise and have been applied to biochemical measurements<sup>8,9</sup>. The fabrication of structures that combine these disparate electronic properties has resulted in exotic devices for a variety of applications from tunnel FETs<sup>10</sup> to scalable quantum resistance standards<sup>11,12</sup> that have dramatically increased performance over conventional Si-FETs—and heterostructures from atomically thin films used in optoelectronic applications.<sup>13–15</sup> The atomically thin electronic channels enabled by 2D materials allow the fabrication of ultra-thin body devices that are controlled by top- and back-gate stacks, resulting in devices that amplify small biochemical signals while also improving the measurement resolution.<sup>16,17</sup> With an increasing focus on wafer-scale growth of novel 2D materials,<sup>18</sup> the route to CMOS compatible fabrication appears relatively straightforward. However, outstanding issues with device fabrication and processing,<sup>19</sup> and reliable growth of gate dielectrics<sup>9</sup> must first be solved.

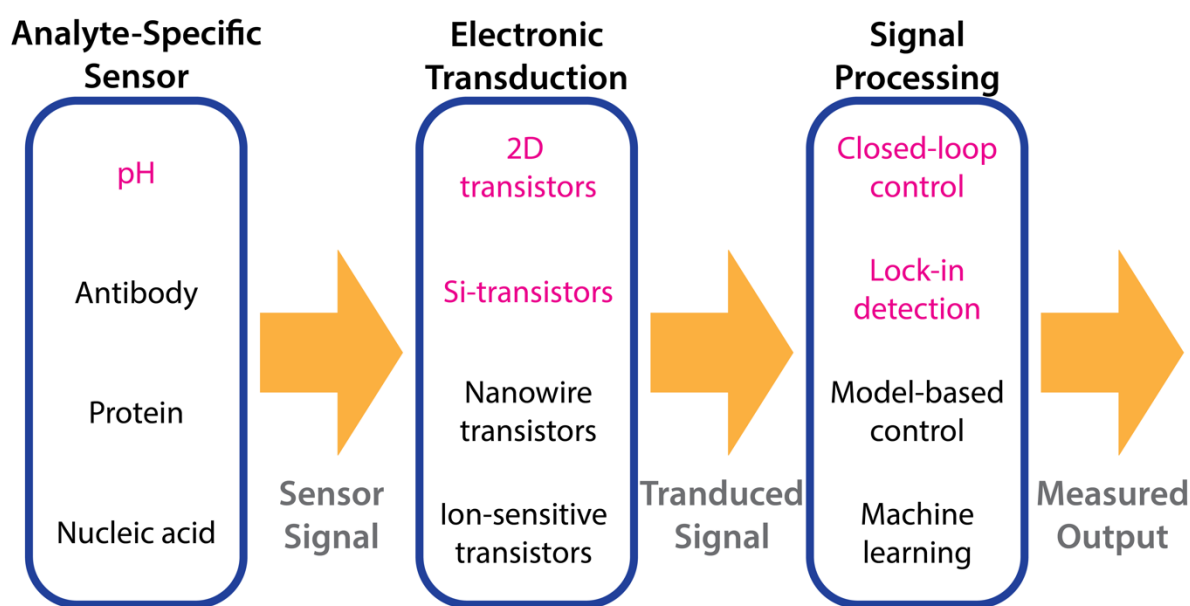


**Figure 1:** General principle of electronic biochemical measurements. Sensitive bioreceptors on sensors interact with target analytes. The signal is transduced resulting in a measurable response that can be further processed and displayed.<sup>20</sup> The text in pink highlights the specific sensors, transduction, and signal processing approaches utilized in this work.

Techniques that leverage novel new transducers have also led to measurement configurations that greatly increase the scalability, stability, and reusability of FET-based transducers. These approaches include

structural modifications to traditional FET devices to result in ion-sensitive field-effect transistors (ISFETs) in modified CMOS processes,<sup>21,22</sup> floating-gate FETs that have found application in DNA sequencing,<sup>23</sup> and extended-gate<sup>24,25</sup> and dual-gate FETs.<sup>17,19,26</sup> Our recent efforts have focused on using dual-gate FETs fabricated with atomically thin MoS<sub>2</sub> channels to improve pH resolution for applications in therapeutic discovery for neurological conditions such as Alzheimer’s disease.<sup>16,17</sup> The devices allow the amplification of pH signals by  $\approx 75$ -fold<sup>16</sup> over the Nernst value of 59 mV at room temperature. A critical element of our approach is to combine novel transistor structures with common signal processing techniques adapted from other research areas to significantly improve the overall performance of the complete sensor system.

Our techniques, described in this paper, utilize closed-loop proportional-integral-derivative (PID) control to operate devices at peak sensitivity. This combination allows us to improve the performance of both state-of-the-art devices fabricated with 2D materials and commercially sourced Si FETs. As a further improvement to performance, we show that the pH resolution of Si-FETs can be further increased by integrating lock-in amplifiers (LIA) to recover weak signals. The common signal processing approaches highlighted here are compatible with integration within microcontrollers for a wide range of applications. PID controllers are widely used to control process variables for increased stability and accuracy by continually adjusting a process parameter in response to deviations from a pre-determined set-point.<sup>27</sup> The approach is commonly used in many applications to control temperature sensors,<sup>28</sup> gas detectors,<sup>29–34</sup> photosensors,<sup>35</sup> hydrogen sensors,<sup>36,37</sup> and to improve the reproducibility and accuracy of atomic force microscopy (AFM) by controlling gain parameters.<sup>38–41</sup> LIAs are also broadly used to measure periodic signals in the presence of substantial noise and improve the measurement signal-to-noise (SNR).<sup>42,43</sup> In particular, the approach leverages the fact that signals need to be recovered under narrow bandwidth conditions, whereas noise processes are typically broadband. Therefore, exciting the device under test at a specific frequency allows the detection of a signal over a narrow bandwidth of interest, while rejecting broadband background noise.<sup>44</sup> This remarkable ability has resulted in LIAs being commonly used in optical and radio frequency (RF) cavities to lock onto resonances,<sup>45–47</sup> sensitive gas sensors,<sup>48</sup> and microfluidic impedance measurements.<sup>49</sup> Combining these approaches can result in significant performance gains in FET-based measurement systems as we will show in this work.

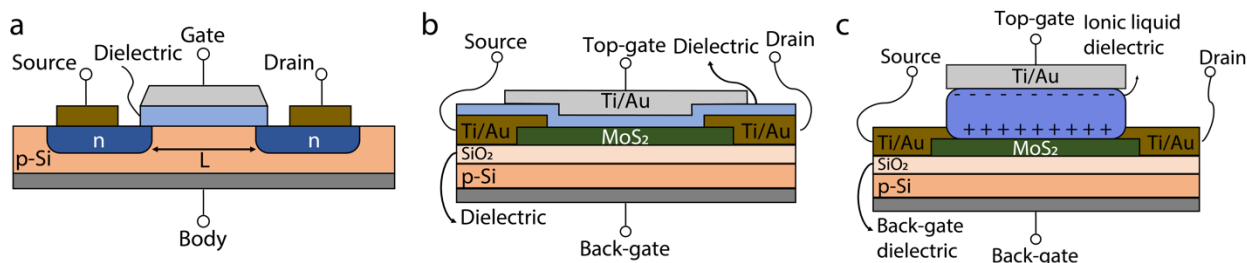


**Figure 2:** Single-gate and dual-gate field-effect transistor (FET) transducers for use in biochemical measurements. (a) Schematic of commercially sourced single-gate FET transducers. Biochemical signals applied to the top gate modulate the current in the semiconducting channel. (b) Schematic of solid-state dual-gate FET (SS-dgFET) transducers formed from atomically thin monolayer MoS<sub>2</sub> channels. (c) Schematic of an ionic-liquid dual-gate FET (IL-dgFET) transducer. The top-gate is formed by contacting an ionic-liquid which is on top of an atomically thin monolayer MoS<sub>2</sub> channels. Biochemical signals are applied to the top gate of the dual-gate FETs and amplified in

proportion to the applied charge due to strong coupling between the top and back gate *via* the semiconducting channel.

In the following sections of this paper we will describe technical details of our high-performance sensor systems that have unparalleled pH sensing resolution for use in biochemical measurements. At the heart of these systems are FET devices. We have shown that both novel 2D FETs and conventional single-gated FETs (illustrated in Figure 2) can be successfully used within these sensor systems. Below, we detail our experimental process, data analysis, and instrumentation. More specifically, we will review the process of fabricating state-of-the-art dual-gated FETs based on atomically thin 2D materials. We will then describe the approaches to electrically characterize the basic FET properties and determine their optimal operating points for sensing. After explaining how to combine these FETs with appropriate feedback and signal processing electronics to create a complete sensor system, we will describe methods to fully characterize the system and determine its overall performance. In the process, we will describe how each aspect of the system contributes to creating a complete sensor system with remarkable performance. Near the end, we also discuss additional optimization and signal recovery techniques that further improve our sensor performance.

## 2. Top- and Bottom-Gated 2D FETs

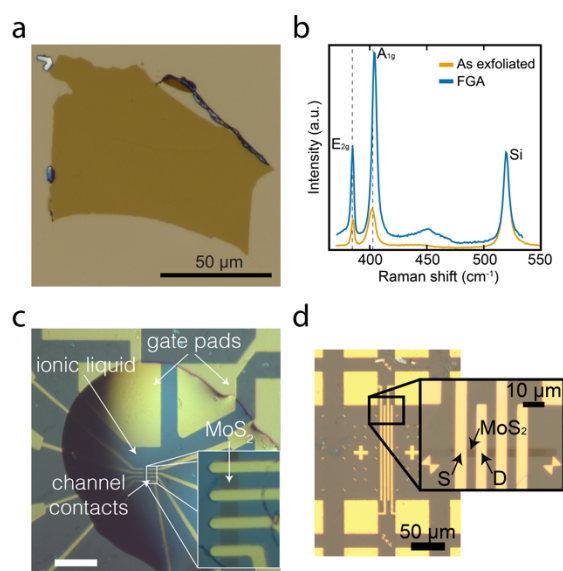


**Figure 3:** Fabrication of dual-gate field-effect transistors (FET) formed with atomically thin MoS<sub>2</sub> channels. (a) Large area ( $\approx 5000 \mu\text{m}^2$ ) monolayers of MoS<sub>2</sub> were exfoliated and transferred to a SiO<sub>2</sub> on Si substrate. (b) Raman spectra of the MoS<sub>2</sub> monolayer before (*orange*) and after (*blue*) a cleaning step validates<sup>19</sup> chemical and physical properties of the film. (c) A room-temperature ionic liquid used as the top-gate dielectric enabled dual-gate FETs for high-sensitivity measurements of biomolecules. The scale bar represents  $100 \mu\text{m}$ . (*inset*): Detailed view of the FET array. (d) Optical image of a representative array of solid-state dual-gate FETs prior to deposition of the top-gate dielectric and top-gate metal. (*inset*): Detailed view of the FET array. *Panels a, b and d:* Adapted with permission from *ACS Appl. Mater. Interfaces* **11**, 16683–16692 (2019). Copyright 2019 American Chemical Society. *Panel c:* *Nanoscale* **11**, 15622–15632 (2019) – Adapted with permission of The Royal Society of Chemistry.

When properly designed, transistors with both a top gate and a bottom gate can amplify sensor signals and greatly improve the performance of sensor systems. For example, in pH measurements, dual-gate FETs can amplify pH signals considerably over the Nernst value of 59 mV at room temperature. We have designed and made different types of FETs based on 2D materials with both top and bottom gates to demonstrate and explore the limitations of this amplification. In solid-state dual-gate 2D FETs (SS-dgFETs, Figures 2b and 3d) the back gate consists of a doped Si wafer with a high-quality thermally grown SiO<sub>2</sub> layer as the back-gate dielectric. In these solid-state devices, the top-gate dielectric is aluminum oxide. Ionic liquid-gated dual-gated 2D FETs (IL-dgFETs, Figures 2c and 3c) use a unique approach to form the top-gate dielectric that relies on a room temperature ionic liquid. Each of these device types has distinct advantages for sensing applications that are discussed in subsequent sections.

**2D Dual-Gate Transistor Fabrication.** We present here a brief overview of the methods used to fabricate S-dgFET and IL-dgFETs. Detailed descriptions of the fabrication processes were previously presented.<sup>16,17,50,51</sup> Monolayer MoS<sub>2</sub> was first transferred onto an oxidized Si substrate (SiO<sub>2</sub> with a thickness of 70 nm or 300 nm) by using a gold-mediated exfoliation technique.<sup>21</sup> Figure 3a shows a representative optical image of monolayer MoS<sub>2</sub> films obtained by using this method. The thickness (monolayer) and composition of the transferred material were confirmed with Raman spectroscopy (Figure 3b).<sup>13</sup> Optical lithography was then used to pattern source (*S*) and drain (*D*) contacts onto the film, followed by electron-beam metal deposition (80 nm Au on 2 nm Ti) and metal lift-off in acetone (Figures 3c and 3d). A second optical lithography step was used to photolithographically define a 5 μm × 5 μm channel for each FET. The excess 2D film was etched with a XeF<sub>2</sub> process. The devices were annealed under forming gas (5 % H<sub>2</sub>, 95 % Ar) for 24 hours to minimize organic contamination and improve the contact resistance of the FETs.<sup>13</sup> The large areas and relative abundance of exfoliated monolayers transferred onto the substrate with Au-mediated exfoliation allowed batch fabrication of numerous monolayer FET arrays on a 4-inch wafer.

For SS-dgFETs with solid-state front and back gate dielectrics, a 20 nm top-gate (*TG*) Al<sub>2</sub>O<sub>3</sub> dielectric was deposited by using atomic layer deposition (ALD) immediately after the forming gas annealing step. Optical photolithography was used to pattern the top-gate metal, followed by electron-beam metal deposition (100 nm Au on 10 nm Ti) and metal lift-off in acetone. A schematic of an SS-dgFETs is depicted in Figure 2b. For IL-dgFETs, a small droplet of the ionic liquid DEME-TFSI IL\* (727679; Sigma Aldrich, St. Louis, MO) is used for top-gating. The droplet was carefully applied onto each group of devices by using a micromanipulator and an optical microscope following the definition of the source and drain contacts. The droplet was sized to overlap the MoS<sub>2</sub> monolayer and the gate electrodes,<sup>31,32</sup> as seen from the schematic representation in Figure 2c and from the optical image of a completed device in Figure 3c. An important consideration in the design of high performing IL-dgFETs is a large ratio of the area of the gate electrode to the combined area of the source, drain contacts, and MoS<sub>2</sub> channel. Finally, in order to confirm that gate leakage in these IL-dgFETs was small relative to the channel current, the

---

\* Certain commercial equipment, instruments, or materials are identified in this paper in order to specify the experimental procedure adequately. Such identifications are not intended to imply recommendation or endorsement by the National Institute of Standards and Technology, nor is it intended to imply that the materials or equipment identified are necessarily the best available for the purpose.

current across the ionic liquid was measured upon application of a potential between two patterned gate electrodes.

### 3. Electrical Characterization

Before the FETs can be used in optimized sensing circuits, they must be parametrically characterized. These properties will also be used to define the FETs' optimal operating set points for sensing applications. In the following section, we will describe the necessary electrical characterization of individual FETs. We describe methods to measure critical device parameters in FETs that have both top and bottom gates and in traditional single-gated FETs.

**Amplification Factor ( $\alpha$ ) for SS-dgFETs and IL-dgFETs.** The SS-dgFETs and IL-dgFETs were electrically characterized following fabrication by using the setup shown schematically in Figure 4a. The transfer characteristics of both device types (SS-dgFET and IL-dgFET) were measured by recording the drain current ( $I_D$ ) as a function of the top-gate potential ( $V_{TG}$  or  $V_{LG}$ ) with a constant drain voltage ( $V_D$ ) as seen from Figures 4b and 4d. The asymmetric coupling between the top- and back-gate capacitances<sup>8</sup> *via* the channel will cause a threshold voltage shift in the top gate when a bias is applied to the back gate. To estimate the magnitude of this effect, which results in a signal amplification ( $\alpha$ ), we repeatedly measured the transfer characteristics of each device under varying back-gate biases, as seen from the family of curves in Figures 4b and 4d. For each transfer curve in the figure, we determined the top-gate threshold voltage ( $V_{i,LG}$  or  $V_{i,TG}$ ) from a linear extrapolation of  $I_D(V_{TG})$  at the voltage corresponding to peak transconductance.<sup>23</sup> Figures 4c and 4e plot  $V_{BG}$  against the top-gate threshold voltage, which in turn allowed the determination of the device gain from the expression  $\alpha=dV_{BG}/dV_{i,TG}$  for the SS-dgFETs and  $\alpha=dV_{BG}/dV_{i,LG}$  for the IL-dgFETs.<sup>8</sup> The error bars in the figure report the standard error defined as the standard deviation of the population mean.

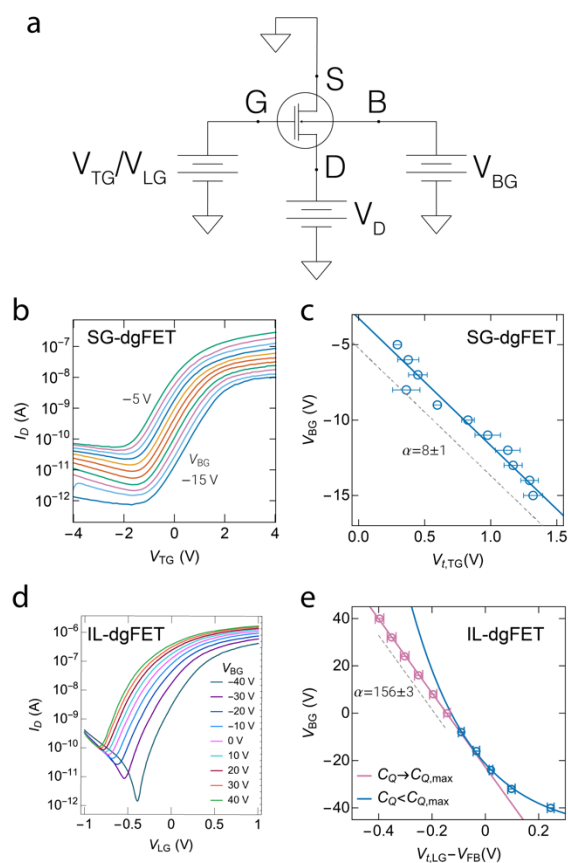


**Figure 4:** Electrical characterization of solid-state dual-gate 2D FETs (SS-dgFETs) and ionic liquid gated 2D FETs (IL-dgFETs). Error bars report the standard error defined as the standard deviation of the population mean. (a) Measurement schematic for electrical characterizing of a monolayer MoS<sub>2</sub> dual-gated FET for remote biosensing. The MoS<sub>2</sub> 2D semiconducting channel spans the source (S) and drain (D) contacts. The source contact is grounded and a constant potential ( $V_D$ ) is applied to the drain contact driving a current ( $I_D$ ) across the 2D channel. The channel conduction is electrostatically controlled by a voltage applied to the silicon substrate ( $V_{BG}$ ), which forms the global back gate or by a voltage applied to the top-gate metal ( $V_{TG}$ ). (b) Transfer characteristics of SS-dgFETs obtained by sweeping  $V_{TG}$  and measuring  $I_D$  as a function of  $V_{BG}$ . (c) The change in  $V_{BG}$  as a function of the top-gate threshold voltage ( $V_{t,TG}$ ) for the SS-dgFETs. A linear regression to the data ( $n=5$ ) is used to determine the signal amplification ( $\alpha$ ) of  $V_{TG}$  at the back gate. (d) Transfer characteristics for the IL-dgFETs obtained similarly to the measurements in panel b. (e) A nonlinear regression to the change in  $V_{BG}$  as function of liquid-gate threshold voltage ( $V_{t,LG}$ ) returns two distinctive regimes: (pink)  $\alpha$  is constant at high positive  $V_{BG}$ , and (blue)  $\alpha$  decreases exponentially at negative values of  $V_{BG}$ . *Analyst* **145**, 2925–2936 (2020); *Nanoscale* **11**, 15622–15632 (2019) – Adapted with permission of The Royal Society of Chemistry.

Figure 4c shows the relationship between  $V_{BG}$  and  $V_{t,TG}$  for SS-dgFETs. The value of  $\alpha$  was determined for these devices by applying a linear regression to the data. The measured SS-dgFET device resulted in  $\alpha = 8 \pm 1$ , which is  $\approx 4$ -fold larger than state-of-the-art dual-gate silicon devices.<sup>15</sup> Figure 4e highlights the relationship between  $V_{BG}$  and  $V_{t,LG}$  for IL-dgFETs. The data was analyzed by using the same procedure to extract  $\alpha$  as above. In this case, we can clearly discern two regimes. At a large and positive  $V_{BG}$  (Figure 4e; pink) the device was in the limit of a large channel carrier density ( $n_{ch}$ ). In this regime,  $\alpha$  has a constant value of  $156 \pm 3$  (back-gate SiO<sub>2</sub>;  $d=300$  nm). At negative  $V_{BG}$ , and therefore low  $n_{ch}$  (Figure 4e; blue),

$\alpha$  decreases exponentially. Both regimes of operation can be explained by a quantum capacitance model that we will discuss next.

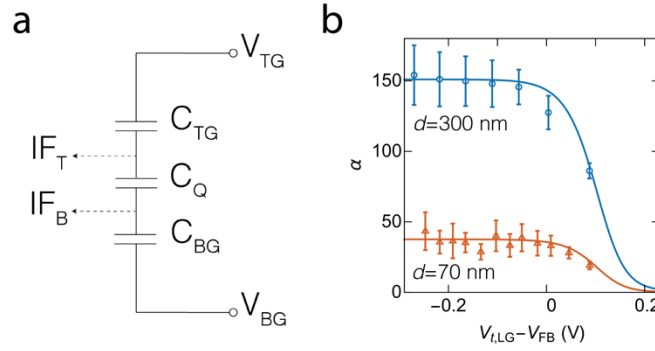


**Figure 5:** Theoretical model and analysis of ionic liquid-gated 2D field-effect transistors (IL-dgFETs). (a) The IL-dgFETs can be described by a simple model comprised of three capacitors in series that represent the top-gate dielectric ( $C_{TG}$ ), back-gate dielectric ( $C_{BG}$ ) and channel quantum capacitance ( $C_Q$ ). (b) The device amplification ( $\alpha$ ) as a function of the ionic liquid-gate threshold voltage ( $V_{t,LG}$ ) is shown for two IL-dgFETs with a 70 nm SiO<sub>2</sub> back-gate dielectric (orange) and a 300 nm SiO<sub>2</sub> back-gate dielectric. *Nanoscale* **11**, 15622–15632 (2019) – Adapted with permission of The Royal Society of Chemistry.

**Quantum Capacitance-Limited Performance.** For dual-gate devices,  $\alpha$  can be estimated from the model in Figure 5a, where  $C_{TG}$  and  $C_{BG}$  are the capacitances associated with the top and bottom-gate dielectrics,  $C_Q$  is the intrinsic quantum capacitance of the channel material, and  $IF_T$  and  $IF_B$  represent the interface between the top-gate dielectric and the channel and the back-gate dielectric and the channel respectively. A quantum capacitance arises when the electric field due to charges on one gate partially penetrates through a thin transistor channel (such as in a 2D FET) and induces charges on the other control gate. This model can be simplified for the SS-dgFETs because the gate oxide capacitances are an order of magnitude smaller than  $C_Q$  for MoS<sub>2</sub>, resulting in  $\alpha \approx C_{TG}/C_{BG}$ .<sup>16,31,40</sup> In this regime,  $\alpha$  is constant, independent of the charge concentration in the channel ( $n_{ch}$ ) and is defined solely by the physical and material properties of the gate dielectric.<sup>35</sup> This constant  $\alpha$  allows us to calculate the theoretical value of  $\alpha$  to be 8.8 for devices with the same geometry as the one whose experimental data is shown in Figures 4b and 4c: a 20 nm Al<sub>2</sub>O<sub>3</sub> top-gate dielectric and 70 nm SiO<sub>2</sub> bottom oxide with identical top and back gate areas. Furthermore, this theoretical estimate of  $\alpha$  is consistent with the measured value of  $8 \pm 1$  extracted from Figure 4c.

The simplified model discussed above is not directly applicable for the IL-dgFETs due to the large capacitance associated with the ionic liquid gate dielectric. Therefore,  $C_{TG}$  is limited in this case by  $C_Q$  of the 2D semiconducting channel. Importantly,  $C_Q$  asymptotically approaches its theoretical limit,  $C_{Q,max}$  when  $n_{ch}$  is large and the devices operate in the strong inversion regime.<sup>33</sup> Under these conditions  $\alpha$  is constant and limited by  $C_Q$ . On the other hand, when  $n_{ch}$  is reduced,  $C_Q$  and therefore  $\alpha$  decrease exponentially. This transition between the linear and exponential regimes is clearly observed from Figure 4e and also in the plot of  $\alpha$  shown in Figure 5b for two independent devices with 70 nm and 300 nm back-gate SiO<sub>2</sub>, respectively. Furthermore, the quantum capacitance limited value of  $\alpha$  scales with  $C_{BG}$ , which is consistent with the values of  $156 \pm 3$  for the 300 nm back-gate SiO<sub>2</sub> and  $41 \pm 4$  for the 70 nm back-gate SiO<sub>2</sub>.<sup>16</sup>

**Si-FET Characterization.** Single-gate Si-FETs do not exhibit the signal amplification of dual-gate devices. However, their performance can be improved using the techniques described in this work. Optimal setup of these devices for sensing applications requires parametric characterization to determine their baseline performance. The measurement setup that utilizes Si-FETs is reproduced from our previous work<sup>17</sup> and shown schematically in Figure 6a. The transfer characteristics of the devices (Figure 6b) were obtained by sweeping the gate voltage ( $V_G$ ) and recording the drain current ( $I_D$ ) when the drain voltage ( $V_D$ ) was fixed at a constant value of 100 mV. The Si-FETs exhibit a steep sub-threshold slope of  $\approx 100$  mV per decade at room temperature. The gate leakage current ( $I_G$ ) of the devices was found to be consistently low and well below  $\approx 1$  pA. The device transconductance ( $g_m$ ), estimated by taking the gradient of the transfer curve, is shown in Figure 6b (*inset*). The devices exhibit a peak transconductance ( $g_{m,peak}$ ) of  $\approx 78 \mu\text{S}$  when  $V_G=0.385$  V. These measurements allow optimal setup of the devices for biosensing experiments in a constant current mode as described in the next section.

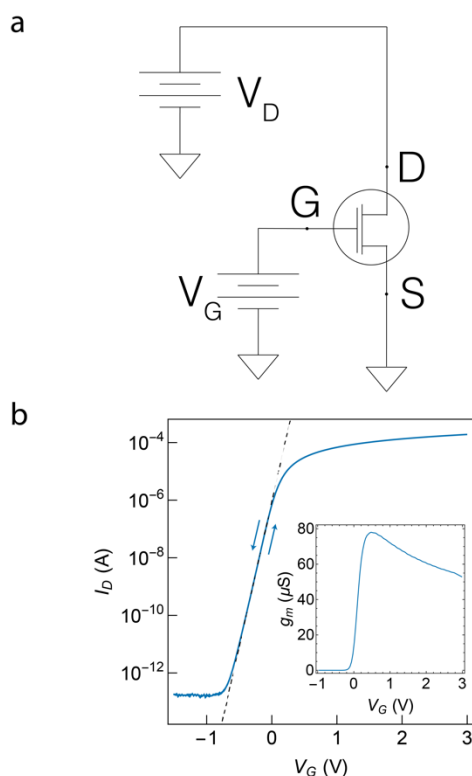


**Figure 6:** Electrical characterization of commercially sourced n-channel Si field-effect transistors (Si-FETs). (a) Measurement schematic of Si-FETs used for remote biosensing measurements. (b) The transfer characteristics obtained by sweeping the gate potential ( $V_G$ ) and measuring the current ( $I_D$ ) between the source (S) and drain (D) terminals. (*inset*): Transconductance of the Si-FETs ( $g_m$ ) as a function of  $V_G$  obtained by taking the derivative  $dI_D/dV_G$ . *Analyst* **145**, 2925–2936 (2020) – Adapted with permission of The Royal Society of Chemistry.

#### 4. Closed-Loop Feedback Control of Single- and Dual-Gate FETs

After a FET is identified and parametrically characterized, it can be integrated into a sensor system. We have found that using closed-loop control greatly improves the system performance. The theoretical

principles for allowing closed-loop control bio-measurements are similar for all three types of FETs discussed here: dual-gate (SS-dgFETs and IL-dgFETs), and single-gate Si-FETs.<sup>16,17</sup> In all cases, the channel current ( $I_D$ ) is maintained at a constant value by continually adjusting a gate voltage. The gate voltage and subsequently  $I_D$  are regulated by closed-loop feedback through a proportional-integral-derivative (PID) controller. The differences in the specific setup for each device arise from their individual structures as shown in Figure 7a and 7b. For the dual-gate 2D-FETs, the controller's output is applied to the back gate of the device and is used to counteract a change in  $I_D$  from a sensor voltage applied to the top gate (Figure 7a). For the Si-FET, which has a single top gate, the control voltage is continually summed with the sensor signal to maintain a constant  $I_D$  (Figure 7b).

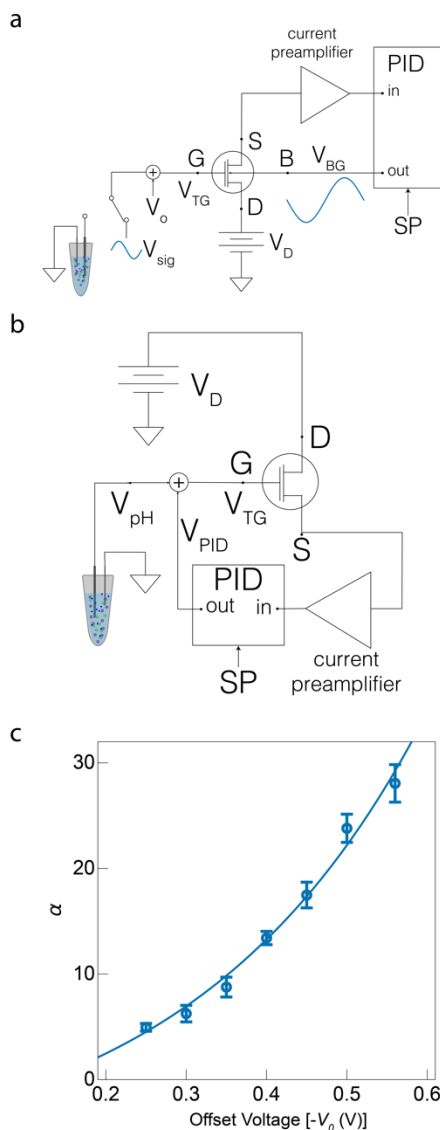


**Figure 7:** Constant current operation of field-effect transistors (FETs). (a) Schematic representation of constant current mode operation of solid-state dual-gate 2D FETs (SS-dgFETs) and ionic liquid-gated 2D FETs (IL-dgFETs).<sup>8</sup> A proportional-integral-derivative (PID) controller was used to maintain the channel current ( $I_D$ ) at a constant value. Control of  $I_D$  was achieved by continually adjusting the back-gate voltage ( $V_{BG}$ ) in response to changes in the top-gate potential ( $V_{TG}$ ) applied either using a waveform generator or from the output of a pH sensor ( $V_{sig}$ ). A DC offset voltage ( $V_o$ ) was summed with  $V_{sig}$  to determine the optimal operation region of the SS-dgFET and IL-dgFETs. (b) Constant current mode operation of the n-channel Si-FETs was performed by using a PID controller to monitor  $I_D$  and continually adjust the PID voltage ( $V_{PID}$ ).  $V_{PID}$  was summed with  $V_{pH}$  prior to being applied to the gate contact

of the Si-FET. (c) Scaling behavior of the IL-dgFETs amplification ( $\alpha$ ) as a function of offset voltage ( $-V_0$ ). *Analyst* **145**, 2925–2936 (2020); *Nanoscale* **11**, 15622–15632 (2019) – Adapted with permission of The Royal Society of Chemistry.

**Measurement Setup:** Time-series data with the Si-FETs, SS-dgFETs or IL-dgFETs were measured with circuits following the schematics in Figure 7a and 7b. For the SS-dgFET and IL-dgFET,  $\alpha$  was measured by connecting the terminal  $V_{SIG}$  to an arbitrary function generator (HF2LI; Zurich Instruments, Zurich, Switzerland). A switch was used to alternate between this calibration and the biosensing signal, for example, obtained with a glass sensitive pH microelectrode (MI-4156; Microelectrodes, Bedford, NH). An offset voltage,  $V_0$ , (GS200; Yokogawa Corporation, Tokyo, Japan), used to determine the optimal operating point of the 2D FET was then added to  $V_{SIG}$  with a summing amplifier (SR560; Stanford Research Systems Inc., Sunnyvale, CA) to result in the potential  $V_{TG}$  applied to the FET top gate. The setup for the Si-FETs is simpler with the output of the PID controller summed with the signal from the biosensing element prior to being applied to the Si-FET gate.

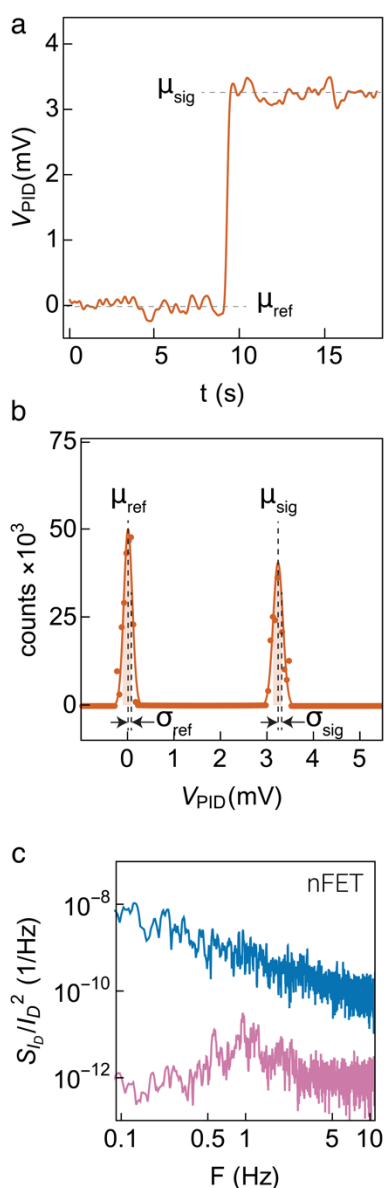


**Figure 8:** Time-series data analysis of pH measurements and power spectral density (PSD) of the channel current. (a) Time-series measurements of the output of the Si-FETs ( $V_{PID}$ ) in response to measurements of buffered pH solutions in constant current mode with a bandwidth,  $B=10$  Hz. The signal was alternatively connected to a reference potential with a mean value,  $\mu_{ref}$  and a signal with a mean value,  $\mu_{sig}$ . (b) A model with two Gaussian functions was fit to the histogram of the time-series data from panel a. The expanded uncertainty ( $k=2$ ) was propagated and used to estimate the pH resolution. (c) PSD of the channel current ( $I_D$ ) of the Si-FETs under open-loop operation (*blue*) and under PID control (*pink*) are shown. *Panel c: Analyst 145, 2925–2936 (2020) – Adapted with permission of The Royal Society of Chemistry.*

All FETs were operated in a constant current mode. A PID controller that varied  $V_{BG}$  (for the SS-dgFET and IL-dgFET) or  $V_{TG}$  (for the Si-FET) in response to changes in  $I_D$ . The channel current was first amplified by using a current preamplifier (DLPCA-200; FEMTO, Berlin, Germany) with a transimpedance gain of  $10^6$  V/A for the SS-dgFET and IL-dgFET, and  $10^3$  V/A for the Si-FET. The amplified voltage was input to a digital PID controller (HF2LI; Zurich Instruments, Zurich, Switzerland), filtered by a 4-pole Bessel low pass filter (LPF) with a bandwidth of 5 kHz and then sampled at 25 kHz with a 14-bit analog to digital converter. The PID controller varied its output voltage in response to changes in  $I_D$  with a bandwidth of 1 kHz ( $K_P=496.1$ ,  $K_I=9.242 \times 10^3$  s $^{-1}$  and  $K_D=8.02$   $\mu$ s). Optimal values of the PID set-point,  $V_0$ , and  $V_D$  were chosen from the transfer characteristics of each FET shown in Figures 4b, 4d and 6b for the SS-dgFET, IL-dgFET and Si-FET respectively.

**Tuning IL-dgFET Sensitivity.** The ability to tune  $\alpha$  of the IL-dgFETs is advantageous in biosensing applications to allow the sensitivity to be offset to obtain a higher dynamic range. This feature is illustrated in Figure 7c, where changing the offset voltage  $V_o$  allowed  $\alpha$  to be tuned smoothly from  $5 \pm 0.4$  to  $28 \pm 1.8$ . In this instance, since the controller maintains a constant  $I_D$ , changing  $V_o$  is equivalent to moving between curves in Figure 4d for a constant current. The maximum value of  $\alpha$  realized in the constant current mode is constrained by the voltage limits of the instrumentation used. However, the measured values of  $\alpha$  were consistent with the quantum capacitance model, and more than an order of magnitude higher than dual-gate silicon FET measurements.<sup>16</sup> Importantly, the ability to smoothly tune sensitivity with only an offset voltage allows a straightforward mechanism to optimize the measurements for a particular application with the highest sensitivity of the IL-dgFETs achieved when they are operated near the linear regime determined from Figure 4e.

**Data Analysis, Measurement Noise and Resolution:** Two independent methods are used to estimate the measurement resolution of a biochemical signal applied to the top gate of all devices described in this study. The first method uses time-series data (Figure 8a) obtained by using the constant current mode from Si-FETs, IL-dgFETs or SS-dgFETs. The devices are switched between a reference state characterized by a mean PID voltage ( $\mu_{ref}$ ) and noise standard deviation ( $\sigma_{ref}$ ), and a signal with mean PID voltage ( $\mu_{sig}$ ) and noise standard deviation ( $\sigma_{sig}$ ) resulting in a step change in the time-series seen in Figure 8a. The two states are characterized by taking the histogram of the time-series as shown in Figure 8b. A functional form that comprises two Gaussian distributions is fit to the data to estimate the parameters of the

distribution. The change in the signal with 95 % confidence is estimated by propagating errors from the underlying Gaussian distributions, resulting in  $\Delta V_{PID} = \mu_{ref} - \mu_{sigma} \pm 2 \sqrt{\sigma_{ref}^2 + \sigma_{sig}^2}$ .

The second approach to analyzing the measurement resolution is by measuring the power spectral density (PSD) of the channel current noise,  $S_{ID}$ , as illustrated in Figure 8c for Si-FET. Under open-loop operation (Figure 8c; *blue*), the devices exhibit a  $1/f$  noise scaling as observed by others in the literature.<sup>15,26</sup> The root mean squared (RMS) noise of the channel current ( $\delta I_D$ ) is then determined from the expression  $\sqrt{\int_{BW} S_{ID} df}$ . For this open-loop example, the RMS noise is  $\approx 2.5$  nA for a bandwidth of 10 Hz. The measurement resolution, typically reported at 10 dB or a SNR of  $\approx 3$ , is 7.5 nA. The PID controller greatly suppresses  $1/f$  noise as seen from Figure 8c (*pink*). When operating under PID control, we found  $\delta I_D$  to be 0.18 nA, which is an order of magnitude lower for a bandwidth of 10 Hz and results in a resolution of  $\approx 0.5$  nA at 10 dB for the Si-FETs. A similar improvement in the channel current noise relative to the open-loop case is also observed for the SS-dgFETs and IL-dgFETs when operating under PID control.

**Sensitivity and Resolution:** The sensitivity of a measurement system is defined as the change in amplitude of the electrical signal (in our case, the top- or back-control-gate voltages) that is measured per unit change of the analytes (which in our example is pH). In general, higher sensitivity measurement systems are preferred. They produce a larger signal change per unit change of the analyte when compared to the output signal from a lower sensitivity measurement system. The resolution of a measurement system is the smallest change in the analytes that the system can detect. Reaching the highest achievable resolution is the ultimate goal when designing and building a measurement system, especially when the target is to measure minute changes in the analyte. In order to achieve a higher resolution, the measurement system must have both high sensitivity and low intrinsic noise. In other words, it is the SNR that determines the ultimate resolution of a sensor system. A high SNR enables the measurement of small changes in an analyte's concentration and gives a higher confidence level in the measurements. In the next few sections, we describe measurement methods to determine the resolution of sensor systems and demonstrate them for pH measurements. We illustrate how incorporating both closed-loop feedback and LIA can improve the resolution of a sensor system.

The device structures of the SS-dgFETs and IL-dgFETs described here, which form an important version of our pH measurement system, are fundamentally different from silicon-based dual-gated FETs described in previous pH measurement studies.<sup>52,53</sup> In those devices, it was interpreted that two channels were formed and controlled independently by the top and bottom gates. In a constant current mode, when traditional silicon dual-gate devices were operated such that there is an inversion channel at the top and bottom interfaces (e.g. the inversion regime), changes in the gate potential at one interface that drive the corresponding channel into stronger inversion (increasing channel current), cause the other channel to be placed into weak inversion (with a corresponding increase in channel noise). Regardless of the polarity of the applied potential at the sensing gate, the overall channel current noise is dominated by the channel in weak inversion. Channel noise could further limit SNR when the devices are operated in the inversion-depletion regime, for example as demonstrated with ultra-thin body dual-gated silicon FETs.<sup>52</sup> In this case, the noise is dominated by the depleted channel and should result in lower performance compared to the

inversion-inversion regime. Furthermore, this effect becomes more pronounced with increasing gain. As a result, extensive work with such devices has shown no measurable improvement in SNR of silicon devices despite large improvements in the sensitivity.<sup>53</sup> In contrast, ultra-thin channels formed with 2D materials have a single conducting channel that is controlled by both the top gate and the back gate. Because the channel can always be placed in the strong inversion regime, the relative noise is low over a wide range of biasing conditions leading to improved SNR with dual-gated 2D FETs.

## 5. High-Resolution pH Measurements

The signal processing techniques described in the previous section allows optimal signal transduction. This in turn, directly improved the pH resolution for systems based upon Si-FETs, SS-dgFETs and IL-dgFETs. The setup used for pH measurements is shown in Figure 7a for SS-dgFETs and IL-dgFETs, Figure 7b for the Si-FETs. In each case,  $V_{SIG}$  was sourced from a microelectrode pH sensor and applied to the top gate of the devices. In the pH sensing examples, the instrumentation for closed-loop control was setup by using the parameters in Table 1. For each device type, the PID set point was selected from the transfer curves in Figures 4b, 4d, and 6b. For the SS-dgFETs and IL-dgFETs,  $V_0$  was adjusted to the values shown in the table to operate the devices in the inversion region where the relative channel noise was lowest as determined from Figures 4b and 4d. This set point also resulted in the IL-dgFETs operating near their quantum capacitance limit for a maximal  $\alpha$ . For the Si-FETs, the PID set point was determined from the value of  $I_D$  that corresponds with the peak channel transconductance in Figure 6b (*inset*). The measured pH time-series response for each device over a narrow range is shown in Figure 9 (*inset*) and processed by using the approach described in Figure 8.

**Table 1:** Parameters for Example High-Resolution pH Measurements

	<b>PID Set-Point</b> ( $\mu\text{A}$ )	$V_0/V_{PID}$ (V)	<b>pH Sensitivity</b> (mV)	<b>pH Resolution</b> $\times 10^{-3}$	<b>G</b> (V/A)
<b>SS-dgFET</b>	0.1	-1.5	$380 \pm 4$	$3.9 \pm 0.9$	$10^6$
<b>IL-dgFET</b>	0.1	-1	$2080 \pm 50$	$0.3 \pm 0.3$	$10^6$
<b>Si-FET</b>	40.5	0.39	$59 \pm 3$	$7.4 \pm 0.3$	$10^3$

Figure 9a, 9b and 9c show our previous pH measurements of PBS buffer solutions measured with SS-dgFETs, IL-dgFETs and Si-FETs respectively when operated in a closed-loop PID configuration.<sup>16,17</sup> The error bars in the figure represent the expanded uncertainty ( $k=2$ ) in the output voltage. The output voltage was divided by the Nernst potential,  $V_{Nernst}$ , at room temperature to then obtain the pH resolution reported in Table 1 and shown in Figure 9d. The pH sensitivity was highest for the IL-dgFETs ( $\approx 2.1$  V;  $R^2=0.998$ ) operating close to the quantum capacitance limit of the 2D channel, followed by the SS-dgFETs ( $\approx 0.4$  V;  $R^2=0.999$ ). The Si-FETs, which do not benefit from the amplification allowed by the dual-gate devices, returned a pH sensitivity ( $\approx 59$  mV;  $R^2=0.988$ ) that was consistent with the Nernst value at room temperature.

The sensitivity of the devices does not necessarily translate to a linear improvement in resolution due to differing relative noise contributions arising from the device characteristics and dynamics. Therefore, while the IL-dgFETs exhibit a  $\approx 35$ -fold improvement in sensitivity over the Si-FETs the resolution improvement was found to be  $\approx 10$ -fold. Similarly, the  $\approx 6$ -fold increase in the SS-dgFET sensitivity translated to an  $\approx 2$ -fold improvement in resolution. The disparity between sensitivity and performance is partly due to the approximately order of magnitude higher channel mobility of the silicon Si-FET over the SS-dgFETs and IL-dgFETs. The higher Si-FET mobility, which also translates into a higher channel current (see Table 1) and lower relative noise largely offsets the higher sensitivity of the SS-dgFETs allowing comparable resolution for both devices. On the other hand, the considerably higher sensitivity of the IL-dgFETs enables these devices to improve pH resolution over the Si-FETs by a large margin. As we will show later in this work, additional optimization and signal processing can be applied to the Si-FETs to close the performance gap with the IL-dgFETs even further.

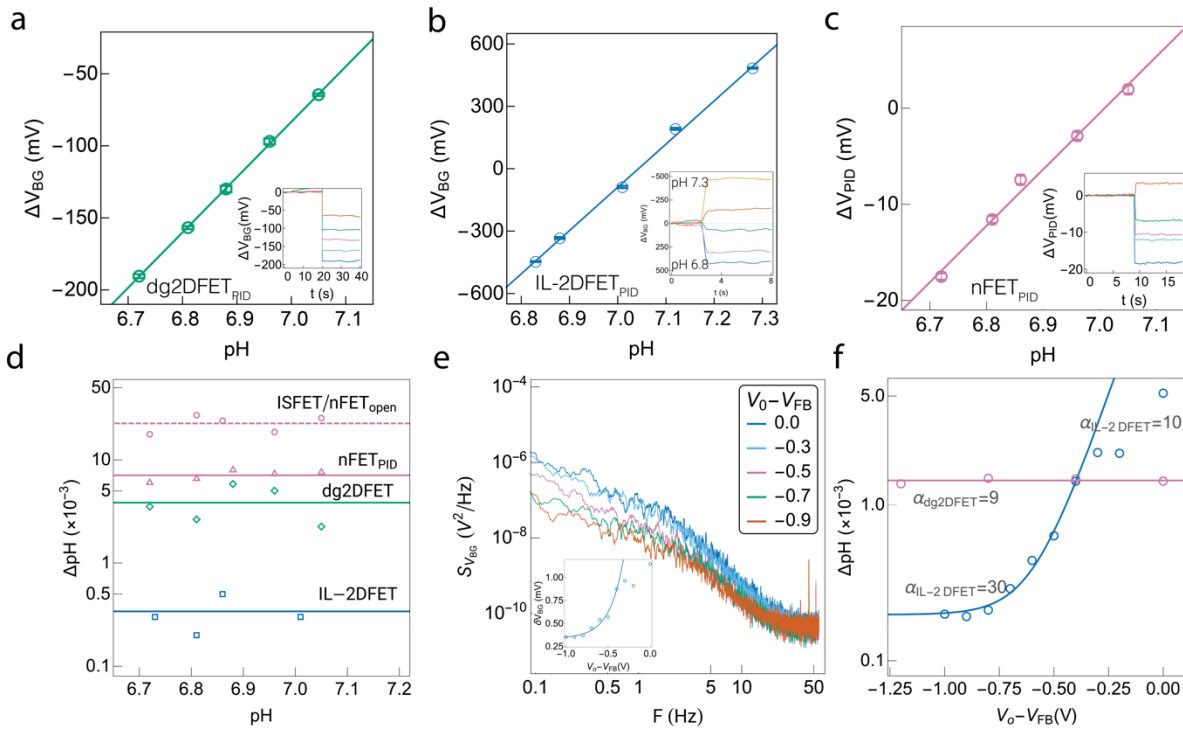


**Figure 9:** pH sensitivity and resolution of research grade dual-gated 2D MoS<sub>2</sub> field-effect transistors (FETs) and a commercially sourced n-channel Si field-effect transistor (Si-FETs). (a), (b), and (c) pH sensitivity measurements made under closed-loop control using solid-state dual-gate 2D FETs (SS-dgFETs), ionic liquid-gated 2D FETs (IL-dgFETs) and Si-FETs respectively. The error bars in all cases represent the expanded uncertainty ( $k=2$ ) of the measured quantity shown on the y-axis of the plot. All measurements were performed with a pH sensitive glass microelectrode. (*insets*): Underlying time-series data for each device that were analyzed to obtain the pH sensitivity plots. (d) A comparison of the pH resolution ( $\Delta pH$ ) of open-loop Si-FETs (pink circle) with IL-dgFETs (blue square) SS-dgFETs (green diamond) and Si-FETs (pink triangle) under PID control. (e) Power spectral density (PSD) of IL-dgFET back gate voltage ( $V_{BG}$ ) for increasingly negative offset voltage ( $V_0$ ). (*inset*): Root-mean-squared (RMS) noise of  $V_{BG}$  as a function of  $V_0$ . (f)  $\Delta pH$  as a function of  $V_0$  for IL-dgFETs (blue) and SS-dgFETs (pink). *Analyst* **145**, 2925–2936 (2020); *Nanoscale* **11**, 15622–15632 (2019) – Adapted with permission of The Royal Society of Chemistry.

We expand on our recent results obtained from devices that have both top and bottom gates to directly compare SS-dgFETs and IL-dgFETs and study their behavior in greater detail. Figure 9e shows representative PSD curves of  $V_{BG}$  for IL-dgFETs with a 70 nm SiO<sub>2</sub> back-gate dielectric as a function of the top-gate offset voltage ( $V_0$ ). The figure shows a reduction in the low-frequency noise in  $V_{BG}$  with increasingly negative  $V_0$ . This behavior is expected because the IL-dgFET increasingly operates in the inversion regime at large and negative values of  $V_0$ , and therefore increasing  $\alpha$ . The broadband noise over the measurement bandwidth (DC to 10 Hz) was determined by integrating each curve in the PSD as described previously. The RMS noise ( $\delta V_{BG}$ ) in  $V_{BG}$  is shown in Figure 9e (*inset*) decreases exponentially with negative  $V_0$  (increasing  $\alpha$ ) before reaching a steady-state value at  $V_0 \approx -1$  V ( $\alpha=30$ ).

The reduction in  $\delta V_{BG}$  with increasing  $\alpha$  directly translates into an improvement in pH resolution ( $\delta pH$ ) of the IL-dgFETs as shown in Figure 9f (*blue*) and was estimated with the expression  $\delta V_{BG}/(\alpha \times V_{Nernst})$ . The pH resolution of the IL-dgFETs was  $0.3 \times 10^{-3}$ , consistent with our previous results.<sup>16</sup> Importantly, the pH resolution is smoothly tunable simply by changing the value of  $V_0$  over a wide voltage range. The results for the SS-dgFETs are markedly different. As discussed previously, these devices do not operate at the quantum capacitance limit. Consequently, they exhibit a constant value of  $\alpha$  while varying  $V_0$  and thereby a constant  $\delta pH$  while operating in the inversion regime of their transfer curve. For the devices shown in Figure 9f (*pink*), this results in a nearly invariant  $\delta pH$  when  $\alpha=9$ . Both devices exhibit higher performance than the Si-FETs. The improved performance is partly the result of the strong coupling of the channel to the gate dielectrics and the resulting amplification. The devices also benefit from a reduction in the low frequency flicker noise by the PID controller, as seen from Figure 8c. This latter point is particularly important because of the low bandwidth of biological signals, which can result in poor measurements limited by low frequency noise. Furthermore, these high-resolution pH measurements directly benefit the measurement of enzyme function at physiological concentrations in buffered aqueous media as we discuss briefly later in this work.

## 6. Solid-State FET Performance Optimization

The performance of the FETs can be further improved by suppressing the low frequency noise over the entire measurement bandwidth. This is partly achieved by using PID control techniques as we have shown previously<sup>17</sup> and reproduced in Figure 8c. Here we show that further improvements are possible by combining lock-in techniques to achieve narrowband detection with the signal processing and control electronics schematically shown in Figure 10a. While LIA's are routinely used to electrically characterize novel FETs, a unique feature of our approach is that we combine signal recovery enabled by the LIA with the additional noise suppression possible by using PID control at signal frequencies below 10 Hz. While the results illustrate the advantages of this approach for Si-FETs, the same techniques can also be applied for the SS-dgFETs. Unfortunately, lock-in techniques are not easily applicable to the IL-dgFETs because of the extremely slow response of the ionic liquid top-gate dielectric as shown in our earlier work.<sup>16</sup> Developments in spin-coated ionic liquids can allow faster response and may allow us to integrate lock-in measurements with IL-dgFETs in future work.<sup>54</sup>

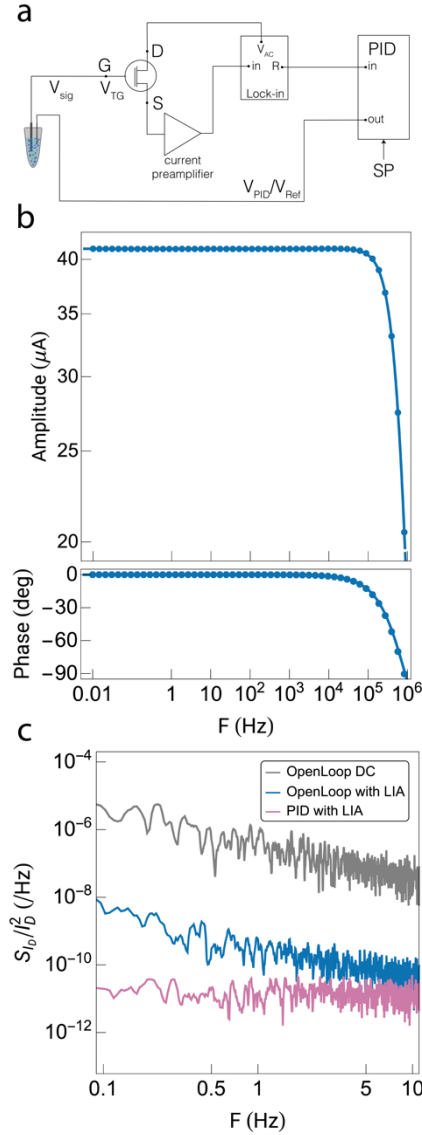


**Figure 10:** Optimal setup and characterization for ultra-sensitive pH measurements. (a) Measurement schematic of closed-loop pH measurements using proportional-integral-derivative (PID) coupled with narrowband detection using a lock-in amplifier. (b) Optimal parameters of the lock-in amplifier were determined by measuring the system dynamics using the swept sign technique, which resulted in both the amplitude (*top*) and phase (*bottom*) response. (c) The power spectral density (PSD) of broadband open-loop measurements (*gray*), open-loop measurements with a narrowband lock-in detection (*blue*) and combining PID and lock-in detection (*pink*) highlight improvements in the relative noise when using narrowband detection.

In our approach, an AC reference signal is first applied to the drain terminal of the Si-FET. The resulting current,  $I_D$ , was first converted to a voltage prior to input to the LIA using a current amplifier with a transimpedance gain,  $G=10^3$  V/A. The LIA was then used to demodulate this AC signal, allowing narrowband detection. The output of the LIA was then connected to the PID controller ( $K_P = 553.5$  mV,  $K_I = 9.22 \times 10^3$  s $^{-1}$  and  $K_D = 10.4$   $\mu$ s), which regulated the gate voltage to maintain a constant current as described previously. The choice of AC reference frequency was determined by first measuring the dynamics of the system, as shown in Figure 10b. The swept sine measurements in the figure are well approximated by a second order transfer function of the form  $\frac{I_0 \omega_c^2}{\omega_c^2 + 2 \omega_c s + s^2}$ , where  $\omega_c$  is the cut-off

frequency,  $I_0$  is the channel current at DC and  $s$  is the complex frequency. A nonlinear regression of the second order transfer function to the data in Figure 8b yielded  $\omega_c=138.5$  kHz and a DC current of  $I_0=41.05$   $\mu\text{A}_{\text{RMS}}$ . The bandwidth limitations likely arise from instrumentation in the measurement chain rather than the Si-FET. The high available bandwidth, relative to that of the measurement signal, allows us to select an AC reference frequency for the LIA of 100 kHz with negligible attenuation. A similar analysis of the SS-dgFET yielded comparable performance.

The benefits of narrowband detection with the LIA are apparent from the PSD of the Si-FET channel current shown in Figure 10c. When compared with open-loop DC operation (Figure 10c; *gray*), the channel noise when using the LIA (Figure 10c; *blue*), obtained by integrating the PSD as before, is reduced by  $\approx 30$ -fold. Furthermore, over the desired signal bandwidth of 10 Hz, the choice of LIA time-constant has little effect on the channel noise (*data not shown*). Therefore, we are able to select a fast LIA time constant of 200  $\mu\text{s}$  ( $B=5$  kHz) to accommodate a PID controller with a 1 kHz bandwidth. Adding a PID controller to the signal processing chain results in a further suppression of noise at very low frequencies (Figure 10c; *pink*). This noise suppression, in turn results in a performance improvement of  $\approx 110$ -fold over the open-loop DC measurements. The drastic performance improvements that result from optimized signal processing improve biological measurement sensitivity. The application of this optimized approach to pH measurements is discussed next.

***Ultra-Sensitive pH Measurements with Lock-in Detection and PID Control:*** We demonstrate improved pH resolution with Si-FETs operated using the schematic in Figure 10a and with the parameters described above. The measurements were performed with a tungsten needle coated with a 100 nm pH-sensitive TiN film. The top gate of Si-FET was connected to the TiN sensing needle immersed in buffered pH solutions. An Ag/AgCl reference electrode, immersed in the solution, was connected to the output of the PID controller ( $V_{ref}$ ) and used to adjust the gate potential,  $V_{TG}$  to maintain a constant channel current. All measurements were performed in a constant current mode using the PID controller and with the LIA used for narrowband detection as discussed above.

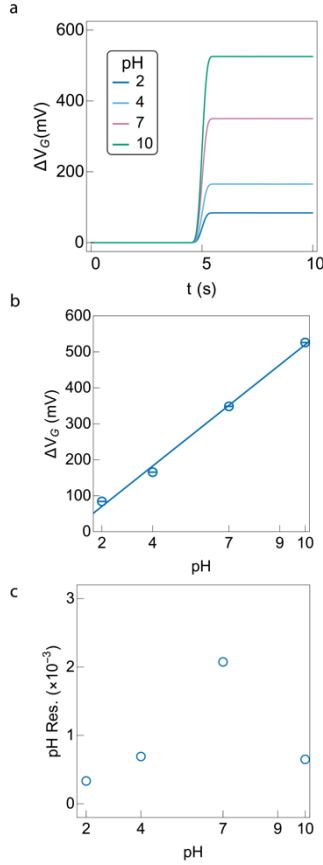


**Figure 11:** Ultra-sensitive pH measurements obtained with n-channel Si field-effect transistors (Si-FETs) operated with proportional-integral-derivative (PID) control and lock-in detection. (a) Time-series measurements of the gate voltage ( $V_G$ ) of Si-FETs operating with lock-in detection and PID control as a function of the buffered solution pH. (b) The pH response of Si-FETs operating in constant current mode with a bandwidth of 10 Hz. (c) The resolution of Si-FETs as a function of pH buffer solutions.

Figure 11a shows the time-series measurements of a Si-FET operating in constant current mode with lock-in detection for pH values ranging from 2 to 10. Similar to previous measurements, the data show a step change in the signal upon connection of the Si-FET gate to the TiN pH sensor. Analyzing these time-series data allowed us to determine the pH sensitivity of the measurements to be  $dV_G/dpH=56$  mV ( $R^2=0.993$ ), consistent with our previous results in Figure 9. Furthermore, the extracted pH sensitivity was comparable to the Nernst value of 59 mV at room temperature.

Noise analysis of the time-series data following the procedure described earlier (see Figure 8 and associated description) allowed us to determine the pH resolution for each measured solution as seen from Figure 11c. As seen from the figure, the pH resolution of the Si-FET was found to be as low as  $0.33 \times 10^{-3}$  at pH 2 (comparable with the IL-dgFET results) and as high as  $2.1 \times 10^{-3}$  for pH 7. The average pH resolution was found to be  $0.9 \times 10^{-3}$ , only a factor of 3 larger than the value obtained with the IL-dgFET and  $\approx 25$ -fold better than open-loop ISFET devices.<sup>55</sup> The results clearly demonstrate the ability of using optimized signal recovery techniques to dramatically improve the SNR of commercially sourced Si-FETs for ultrasensitive pH measurements. Furthermore, the techniques demonstrated here can be directly

applied to research grade devices such as SS-dgFETs or other traditional electronic devices such as bipolar junction transistors for broad adoption.

**Measurements of Enzyme Function and Therapeutic Development:** To demonstrate the effectiveness of the sensors highlighted in this work for biochemical measurements, we previously demonstrated the rapid and sensitive quantification of the function of the enzyme, Cdk5 (protein data bank structure 1UNL<sup>56</sup>) that is implicated in Alzheimer’s disease, and its functional regulation with therapeutic polypeptides.<sup>16,17</sup> The central measurement principle of the approach is that Cdk5 catalyzes the phosphorylation of substrate proteins such as histone H1 through the transfer of a single phosphate group during adenosine triphosphate (ATP) hydrolysis in the presence of an activator protein (e.g., the pathological p25). The reaction releases a single proton into solution, thereby changing the local pH by a very small amount. By measuring this local pH change, we estimated the activity of Cdk5 to be  $(8.2 \pm 1.3) \mu\text{M}$ , consistent with measurements performed using a  $\gamma\text{-}^{32}\text{P}\text{-ATP}$  assay and with values found in the literature.<sup>16</sup> Importantly, the resolution of our approach allows measurements at physiological concentrations of Cdk5 ( $\approx 18 \text{ nM}$ ) using Si-FETs and up to 5-fold below physiological levels using IL-dgFETs.<sup>16,17</sup> The high time-resolution of our technique allowed real-time measurements of Cdk5-mediated phosphorylation of histone in order to determine the kinetics of the reaction. Finally, our approach enabled quantitative and label-free measurements of the re-regulation of Cdk5 by polypeptides such as p5 as a potential drug candidate for Alzheimer’s disease.<sup>17</sup> Further analysis of our measurement noise characteristics and system dynamics allows us to broadly improve performance as discussed below.

**Discussion of Sensing Performance:** We performed a comprehensive experimental characterization of three types of FETs for use as high performance signal transducers in biochemical sensing measurements. While each device-type possesses distinct advantages, robust closed-loop signal processing techniques, enabled by well-established instrumentation, will drastically improve the sensing performance in each case. The general applicability of these signal processing techniques makes them suitable for broad adoption with numerous other electronic transducers for use in biosensing applications.

Commercially sourced Si FETs that have been optimized with decades of engineering refinements offer excellent performance due to a high current drive, stable threshold voltages, fast response times and extremely low channel current noise due to optimized interfaces. However, the low voltage gain of these devices due to their single-gate configuration limits their overall sensitivity. In particular for pH measurements, when operating the devices in a constant current mode, they exhibit a unity voltage gain limiting their maximum pH sensitivity to the Nernst value of 59 mV at room temperature. This metric, which may at first appear to be severely constraining, is mitigated by their extremely low noise characteristics. This allows Si-FETs to attain a pH resolution—the ultimate measure of performance—that is comparable to some of the more exotic devices we have tested in this work.

Voltage sensitivity can be improved with dual-gated devices as presented in this work. We demonstrate two types of dual-gate devices. In the first example, we used solid-state thin top- and thick bottom-gate dielectrics and an atomically thin semiconducting channel (SS-dgFETs). The asymmetric capacitive coupling between the two gates and a single semiconducting channel allows the potential detected by a biosensor connected to the top gate to be amplified. Furthermore, in constant current mode, we operated

the device in the strong inversion regime resulting in low-noise performance. The net result is that the pH resolution was improved by  $\approx 3$ -fold over that of Si-FETs. In the second dual-gated FET example, we replaced the solid-state top gate with a room temperature ionic liquid (IL-dgFETs). In this case, the high intrinsic quantum capacitance of 2D materials coupled with the very large capacitive coupling of the ionic liquid to the semiconducting channel allowed us to achieve voltage sensitivities that to greatly exceed (by up to  $\approx 75$ -fold) the Nernst value. Furthermore, because the sensitivity is dependent on the carrier concentration within the channel, we were able to smoothly tune the amplification by using only an offset voltage. The combination of high sensitivity and operation within the strong inversion regime allowed the measured pH resolution to exceed that of the SS-dgFET by more than an order of magnitude.

Despite the many advantages of dual-gated FETs, they remain research grade devices that can suffer from slow response, low carrier mobility, high contact resistance, and low-quality oxide interfaces. The performance of these devices can be considerably improved by addressing some of these outstanding problems. An ideal transducer will combine the high-sensitivity of dual-gate FETs with the reliability and low noise performance of Si-FETs. The techniques outlined in this work will allow the performance of such an idealized device to be optimized, enabling numerous applications in biotechnology and biophysics.

## 7. Conclusions

We have demonstrated that robust signal processing techniques enabled by well-established instrumentation can drastically improve the performance of both state-of-the-art FETs and commercial devices for applications in biomolecular sensing. We reviewed our recent results applying closed-loop PID control to research-grade FETs fabricated with atomically thin semiconducting channels. The combination of dual-gated device structure, which allows robust signal amplification, combined with signal processing allowed the demonstration of pH resolution of  $92 \times 10^{-6}$  with IL-dgFETs, an  $\approx 35$ -fold improvement over commercial ISFETs. We then showed that when the techniques developed for the dual-gated FETs were adapted for use with commercially sourced Si-FETs they resulted in an  $\approx 5$ -fold improvement in resolution over ISFETs. We leveraged the high performance of both device types to quantitatively measure the function of the Cdk5, an enzyme implicated in Alzheimer's disease, at physiological concentrations and observed its regulation by custom polypeptide therapeutic targets.

We built upon our initial results to further optimize Si-FET performance for biomolecular measurement applications by performing narrowband detection with lock-in amplifiers in conjunction with PID control. The inherently low bandwidth of biological signals, where the flicker noise of the devices dominates, can result in low SNR measurements particularly at small analyte concentrations. This behavior can be improved by utilizing narrowband detection with LIAs that have been commonly used in other areas of research. When combined with the noise suppression capabilities of PID control such a setup can result in a further improvement in pH resolution of almost an order of magnitude when compared with Si-FETs operated without a LIA. Finally, we demonstrated this high performance by using only commercially sourced devices and instrumentation, potentially lowering the bar for the use of our techniques by other researchers.

## Data Availability Statement

The data that support the findings of this study are available from the corresponding author upon reasonable request.

## Acknowledgements

We would like to thank Sufi Zafar from IBM Watson Research Center for providing us with TiN needles for pH measurements. S.T.L. acknowledges support by the National Institute of Standards and Technology (NIST) grant 70NANB16H170. Research performed in part at the NIST Center for Nanoscale Science and Technology nanofabrication facility.

## References

- <sup>1</sup> T. Vo-Dinh and B. Cullum, *Fresenius J. Anal. Chem.* **366**, 540 (2000).
- <sup>2</sup> R. Rapini and G. Marrazza, *Bioelectrochemistry* **118**, 47 (2017).
- <sup>3</sup> C.I.L. Justino, A.C. Duarte, and T.A.P. Rocha-Santos, *Sens. Switz.* **17**, (2017).
- <sup>4</sup> H.W. Wen, in *Handb. Food Chem.* (Springer Berlin Heidelberg, 2015), pp. 1103–1136.
- <sup>5</sup> M.A. Cooper, *Nat. Rev. Drug Discov.* **1**, 515 (2002).
- <sup>6</sup> L.M. Xie, *Nanoscale* **7**, 18392 (2015).
- <sup>7</sup> D. Jariwala, V.K. Sangwan, L.J. Lauhon, T.J. Marks, and M.C. Hersam, *ACS Nano* **8**, 1102 (2014).
- <sup>8</sup> W. Choi, N. Choudhary, G.H. Han, J. Park, D. Akinwande, and Y.H. Lee, *Mater. Today* **20**, 116 (2017).
- <sup>9</sup> K.K. Kim, H.S. Lee, and Y.H. Lee, *Chem. Soc. Rev.* **47**, 6342 (2018).
- <sup>10</sup> A.M. Ionescu and H. Riel, *Nature* **479**, 329 (2011).
- <sup>11</sup> N.N. Klimov, S.T. Le, J. Yan, P. Agnihotri, E. Comfort, J.U. Lee, D.B. Newell, and C.A. Richter, *Phys. Rev. B* **92**, 241301 (2015).
- <sup>12</sup> S.T. Le, J.A. Haggmann, N. Klimov, D. Newell, J.U. Lee, J. Yan, and C.A. Richter, *ArXiv190404726 Cond-Mat* (2019).
- <sup>13</sup> N. Huo, J. Kang, Z. Wei, S.-S. Li, J. Li, and S.-H. Wei, *Adv. Funct. Mater.* **24**, 7025 (2014).
- <sup>14</sup> F. Wang, Z. Wang, K. Xu, F. Wang, Q. Wang, Y. Huang, L. Yin, and J. He, *Nano Lett.* **15**, 7558 (2015).
- <sup>15</sup> A.J. Biacchi, S.T. Le, B.G. Alberding, J.A. Haggmann, S.J. Pookpanratana, E.J. Heilweil, C.A. Richter, and A.R. Hight Walker, *ACS Nano* **12**, 10045 (2018).
- <sup>16</sup> S.T. Le, N.B. Guros, R.C. Bruce, A. Cardone, N.D. Amin, S. Zhang, J.B. Klauda, H.C. Pant, C.A. Richter, and A. Balijepalli, *Nanoscale* **11**, 15622 (2019).
- <sup>17</sup> S.T. Le, M.A. Morris, A. Cardone, N.B. Guros, J.B. Klauda, B.A. Sperling, C.A. Richter, H.C. Pant, and A. Balijepalli, *Analyst* **145**, 2925 (2020).
- <sup>18</sup> S.Z. Butler, S.M. Hollen, L. Cao, Y. Cui, J.A. Gupta, H.R. Gutiérrez, T.F. Heinz, S.S. Hong, J. Huang, A.F. Ismach, E. Johnston-Halperin, M. Kuno, V.V. Plashnitsa, R.D. Robinson, R.S. Ruoff, S. Salahuddin, J. Shan, L. Shi, M.G. Spencer, M. Terrones, W. Windl, and J.E. Goldberger, *ACS Nano* **7**, 2898 (2013).
- <sup>19</sup> N.B. Guros, S.T. Le, S. Zhang, B.A. Sperling, J.B. Klauda, C.A. Richter, and A. Balijepalli, *ACS Appl. Mater. Interfaces* **11**, 16683 (2019).
- <sup>20</sup> N. Bhalla, P. Jolly, N. Formisano, and P. Estrela, *Essays Biochem.* **60**, 1 (2016).
- <sup>21</sup> M.J. Schöning and A. Poghossian, *The Analyst* **127**, 1137 (2002).
- <sup>22</sup> K.B. Parizi, X. Xu, A. Pal, X. Hu, and H.S.P. Wong, *Sci. Rep.* **7**, 41305 (2017).
- <sup>23</sup> Stefano Lai, Fabrizio Viola, Piero Cosseddu, and Annalisa Bonfiglio, *Sensors* **18**, 688 (2018).
- <sup>24</sup> M. Kaisti, *Biosens. Bioelectron.* **98**, 437 (2017).
- <sup>25</sup> C.-S. Lee, S. Kim, and M. Kim, *Sensors* **9**, 7111 (2009).
- <sup>26</sup> R. Pfattner, A.M. Foudeh, S. Chen, W. Niu, J.R. Matthews, M. He, and Z. Bao, *Adv. Electron. Mater.* **5**, 1800381 (2019).
- <sup>27</sup> Kiam Heong Ang, G. Chong, and Yun Li, *IEEE Trans. Control Syst. Technol.* **13**, 559 (2005).
- <sup>28</sup> E. Grassi and K. Tsakalis, *IEEE Trans. Control Syst. Technol.* **8**, 842 (2000).
- <sup>29</sup> J. Herrán, G. G. Mandayo, I. Ayerdi, and E. Castaño, *Sens. Actuators B Chem.* **129**, 386 (2008).
- <sup>30</sup> J. Herrán, G.G. Mandayo, and E. Castaño, *Sens. Actuators B Chem.* **127**, 370 (2007).
- <sup>31</sup> F.R. Bagsican, A. Winchester, S. Ghosh, X. Zhang, L. Ma, M. Wang, H. Murakami, S. Talapatra, R. Vajtai, P.M. Ajayan, J. Kono, M. Tonouchi, and I. Kawayama, *Sci. Rep.* **7**, 1 (2017).

- <sup>32</sup> J. Leis and D. Buttsworth, *IEEE Trans. Ind. Electron.* **65**, 4338 (2018).
- <sup>33</sup> J. Jaiswal, A. Sanger, P. Tiwari, and R. Chandra, *Sens. Actuators B Chem.* 127437 (2019).
- <sup>34</sup> I. Eisele, T. Doll, and M. Burgmair, *Sens. Actuators B Chem.* **78**, 19 (2001).
- <sup>35</sup> D. Arnold, D. Fuchs, K. Wolff, and R. Schäfer, *Appl. Phys. Lett.* **115**, (2019).
- <sup>36</sup> J.L. Chiang, S.S. Jhan, S.C. Hsieh, and A.L. Huang, *Thin Solid Films* **517**, 4805 (2009).
- <sup>37</sup> P.C. Yao, J.L. Chiang, and M.C. Lee, *Solid State Sci.* **28**, 47 (2014).
- <sup>38</sup> G. Schitter, P. Menold, H.F. Knapp, F. Allgöwer, and A. Stemmer, *Rev. Sci. Instrum.* **72**, 3320 (2001).
- <sup>39</sup> L. Liu, J. Shi, M. Li, P. Yu, T. Yang, and G. Li, *Small* **14**, 1803273 (2018).
- <sup>40</sup> X. Wu, Z. Hao, D. Wu, L. Zheng, Z. Jiang, V. Ganesan, Y. Wang, and K. Lai, *Rev. Sci. Instrum.* **89**, (2018).
- <sup>41</sup> M. Dukic, V. Todorov, S. Andany, A.P. Nievergelt, C. Yang, N. Hosseini, and G.E. Fantner, *Rev Sci Instrum* **88**, 123712 (2017).
- <sup>42</sup> A. Mandelis, *Rev. Sci. Instrum.* **65**, 3309 (1994).
- <sup>43</sup> M.O. Sonnaillon and F.J. Bonetto, *Rev. Sci. Instrum.* **76**, 024703 (2005).
- <sup>44</sup> G. de Graaf and R.F. Wolffenbuttel, in *2012 IEEE Int. Instrum. Meas. Technol. Conf. Proc.* (IEEE, Graz, Austria, 2012), pp. 1745–1749.
- <sup>45</sup> P. Harms, J. Sipior, N. Ram, G.M. Carter, and G. Rao, *Rev. Sci. Instrum.* **70**, 1535 (1999).
- <sup>46</sup> P. LeBoulluec, H. Liu, and B. Yuan, *Am. J. Phys.* **81**, 712 (2013).
- <sup>47</sup> G.A. Stimpson, M.S. Skilbeck, R.L. Patel, B.L. Green, and G.W. Morley, *Rev. Sci. Instrum.* **90**, 094701 (2019).
- <sup>48</sup> A. D’Amico, A. De Marcellis, C. Di Carlo, C. Di Natale, G. Ferri, E. Martinelli, R. Paolesse, and V. Stornelli, *Sens. Actuators B Chem.* **144**, 400 (2010).
- <sup>49</sup> Huang, Geng, Zhang, Chen, Cai, Wang, Zhu, and Wang, *Sensors* **19**, 3519 (2019).
- <sup>50</sup> S. Zhang, S.T. Le, C.A. Richter, and C.A. Hacker, *Appl. Phys. Lett.* **115**, 073106 (2019).
- <sup>51</sup> J.R. Hajzus, A.J. Biacchi, S.T. Le, C.A. Richter, A.R. Hight Walker, and L.M. Porter, *Nanoscale* **10**, 319 (2018).
- <sup>52</sup> T. Wu, A. Alharbi, K.-D. You, K. Kisslinger, E.A. Stach, and D. Shahrjerdi, *ACS Nano* **11**, 7142 (2017).
- <sup>53</sup> J. Go, P.R. Nair, and M.A. Alam, *J. Appl. Phys.* **112**, 034516 (2012).
- <sup>54</sup> F. Zare Bidoky, B. Tang, R. Ma, K.S. Jochem, W.J. Hyun, D. Song, S.J. Koester, T.P. Lodge, and C.D. Frisbie, *Adv. Funct. Mater.* **30**, 1902028 (2020).
- <sup>55</sup> L. Mu, I.A. Droujinine, N.K. Rajan, S.D. Sawtelle, and M.A. Reed, *Nano Lett* **14**, 5315 (2014).
- <sup>56</sup> M. Mapelli, L. Massimiliano, C. Crovace, M.A. Seeliger, L.-H. Tsai, L. Meijer, and A. Musacchio, *J. Med. Chem.* **48**, 671 (2005).